Article

Development and Fabrication of Biocompatible Ti-Based Bulk Metallic Glass Matrix Composites for Additive Manufacturing

Po-Sung Chen [1], **Pei-Hua Tsai** [1], **Tsung-Hsiung Li** [1], **Jason Shian-Ching Jang** [1,2,*], **Jacob Chih-Ching Huang** [3], **Che-Hsin Lin** [4], **Cheng-Tang Pan** [4] and **Hsuan-Kai Lin** [5]

1   Institute of Materials Science and Engineering, National Central University, Taoyuan 32001, Taiwan
2   Department of Mechanical Engineering, National Central University, Taoyuan 32001, Taiwan
3   Department of Materials and Optoelectronic Materials, National Sun Yat-Sen University, Kaohsiung 80424, Taiwan
4   Department of Mechanical and Electro-Mechanical Engineering, National Sun Yat-Sen University, Kaohsiung 80424, Taiwan
5   Department of Materials Engineering, National Pingtung University of Science and Technology, Pingtung 91201, Taiwan
*   Correspondence: jscjang@ncu.edu.tw

Abstract: Ti-based metallic glasses have a high potential for implant applications. The feasibility of a new biocompatible Ti-based bulk metallic glass composite for selective laser melting (SLM) had been examined. Therefore, it is necessary to design a high-glass-forming-ability Ti-based metallic glass (ΔT_x = 81 K, γ = 0.427, γ_m = 0.763), to fabricate a partial glass-formable spherical powder (the volume fraction of the amorphous phase in the atomized Ti-based powders being 73% [size < 25 μm], 61% [25–37 μm], and 50% [37–44 μm]), and establish an SLM parameter (a scan rate of 600 mm/s, a power of 120 W, and an overlap of 10%). The $Ti_{42}Zr_{35}Si_5Co_{12.5}Sn_{2.5}Ta_3$ bulk metallic glass composite was successfully fabricated through SLM. This study demonstrates that the TiZrSiCoSnTa system constitutes a promising basis for the additive manufacturing process in terms of preparing biocompatible metallic glass composites into complicated graded foam shapes.

Keywords: metallic glass (MG); biocompatible; selective laser melting (SLM); additive manufacturing (AM)

1. Introduction

Selective laser melting (SLM) is a promising additive manufacturing (AM) technique. SLM involves the direct fabrication of three-dimensional (3D) metallic parts with complex structures and a high density (higher than 99%) by a high-power density laser beam that melts metallic powders in a vacuum or inert-gas protection system through a computer-aided design (CAD) model [1–4]. The components are fabricated by selective melting and fusing powders within and between the layers. The porous structure and ready-to-use parts are easy to produce. Compared with conventional manufacturing techniques, SLM has a fast cooling rate (10^3–10^5 K/s) during the solidification process [5]. This allows the bulk materials to form very fine nonequilibrium microstructures and improves their mechanical properties [6–8].

SLM can be beneficial in medicine. Its greatest advantage is that it enables one to freely customize and personalize medical products, which can reduce patient recovery time and improve surgical outcomes [9,10]. The ideal bionic metallic implant should possess biocompatibility, a porous structure, osteoconductivity or osteoinductivity, and a suitable strength and stiffness [11]. Conventional implants are usually in a solid block form; they do not have the aforementioned characteristics that SLM does. SLM further offers the advantage of a high cost effectiveness. SLM is more cost-competitive for small-volume, large-variety productions, such as spinal, dental, and bone productions, each of which has a

highly complex shape [9]. The fast fabrication of SLM allows a medical product to be made within several hours, leaving enough time for clinicians to respond to contingencies [12–14]. These characteristics of SLM are difficult to obtain through traditional manufacturing methods.

Metallic materials are often the optimal choice for biomedical implants, especially for hard tissue replacements [15–17], because of their high tensile strength, fracture toughness, and greater suitability for load-bearing than ceramics or polymeric materials [18–21]. Among metallic alloys, titanium and its alloys (e.g., Ti-6Al-4V and Ti-6Al-7Nb) are regarded as the preferred materials and are mostly used for biomedical implants in the fields of trauma and orthopedic surgery [21,22]. However, they still create several problems regarding long-term tribological behavior and have raised some health concerns [23,24]. The major problems for the Ti-6Al-4V implant are the mismatch of the Young's modulus (E) with human bone (human bone: E = 10–30 GPa; Ti-6Al-4V: E = 110–120 GPa) and the release of toxic metallic ions and particles through corrosion or wear processes. The large difference of E causes nonuniform loading of the bone interface in implants, resulting in stress-shielding effects. This increases patient recovery time and changes the bone shape [19,20]. In addition, toxic factors might lead to oversensitivity, immune rejection, and tissue loss. Therefore, researchers have been developing new titanium alloys with suitable mechanical properties and a good biocompatibility for bone implants [25–33].

In the past two decades, a new metallic material category, the amorphous alloy or metallic glass (MG), has attracted research attention for its potential biomedical applications [34–38]. Due to their inherently amorphous properties, these MGs do not have crystal structural defects, such as dislocations, twins, or grain boundaries. MGs also possess a homogenous chemical constitution with a higher hardness, higher strength, lower Young's modulus, larger elastic strain, and much better corrosion resistance compared with their counterpart, crystalline alloys [39–43]. Developments in Ti-based MGs without a toxic element, $Ti_{60}Zr_{10}Ta_{15}Si_{15}$, $Ti_{60}Nb_{15}Zr_{10}Si_{15}$, and $Ti_{42}Zr_{40}Ta_3Si_{15}$, have been found to be superior to crystalline Ti-alloy counterparts from a medical-implant point of view [33,34,39,42]. More recently, studies have reported that a new type of bulk metallic glass foam (BMGF) with the ability to support cell growth [35,36,42] can further reduce the effects of stress shielding and problems with toxic elements. However, through the space holder powder metallurgy method, the BMGFs are able to provide only one fixed porosity in one product, thus still facing limits in their application [31]. On the other hand, the Young's modulus of the Ti-based BMG is around 80 GPa, which is still higher than the Young's modulus of 15–25 GPa in the longitudinal direction of cortical bone [44]. These cannot completely satisfy the requirements of human bone with respect to cellular activity and load bearing. The best solution is to use an AM process by an SLM method to directly fabricate high bionic-gradient porous-implant Ti-based MGs on a CAD data model.

In this study, we attempted to improve the glass-forming ability (GFA) of a $Ti_{42}Zr_{40}Ta_3Si_{15}$ system by adding biofriendly Sn and Co elements. The starting Ti-Zr-Ta-Si alloy has been extensively studied in our laboratory for its in vitro and in vivo biocompatibility [39,42]. This starting alloy is well suited as a metallic biomaterial. The alloy is free of toxic elements Ni and Cu and of the expensive element Pd. Gas atomization was used to prepare fully or partially glass-formable spherical powder with a shape factor of 0.85–1 and a particle size distribution of $d_{50} \leq 45$ μm for the SLM process. The fabrication of Ti-based bulk metallic glass composite (BMGC) through SLM was analyzed.

2. Experimental Procedures

Ingots with a nominal composition of $Ti_{42}Zr_wTa_3Si_xSn_yCo_z$ (w + x + y + z = 55 at %) were prepared by arc melting under a Ti-gettered argon atmosphere. The purity of the raw element was above 99.9%. The ingots were turned over and remelted at least four times to ensure their chemical homogeneity. Ribbon samples were prepared by subjecting the ingot to induction melting and ejecting it onto a water-cooled copper wheel (with a tangent speed of 25 m/s and a gap of 0.2 mm between the quartz nozzle and the wheel

surface) in an argon atmosphere. The microstructure of all ribbons was examined by X-ray diffraction (XRD; D8A, Bruker, Billerica, MA, USA) with monochromatic Cu-Kα radiation. The thermal characteristics (glass transition temperature, T_g, and crystallization temperature, T_x) were measured at a heating rate of 40 K/min with differential scanning calorimetry (DSC; DSC 1, Mettler Toledo, Greifensee, Canton of Zürich, Switzerland). The melting behavior (characterized by the melting point, T_m, and liquidus temperature, T_l) was measured at a heating rate of 20 K/min using high-temperature DSC (HT-DSC; DSC 404 F3, Netsch, Selb, Bavaria, Germany).

The fully or partially glass-formable powders were fabricated by using self-designed gas atomization equipment on the south campus of the Industrial Technology Research Institute, Taiwan. Metal powders obtained by gas atomization have a perfectly spherical shape and a high cleanliness level. The particle size distribution of as-prepared alloy powders was analyzed using a Dry-Type Laser Particle Size Analyzer (Mastersizer 2000, Malvern instruments, Malvern, Worcestershire, United Kingdom). The microstructures of each size-ranged alloy powder were examined using XRD analysis and transmission electron microscopy (TEM; JEM-2100, Joel, Akishima, Tokyo, Japan; operated at 200 kV). The morphology and chemical composition of alloy powders were examined using scanning electron microscopy (SEM; F50 Inspect, FEI, Hillsboro, OR, USA; operated at 25 kV) equipped with an electron dispersive spectrometer.

The gas-atomized powders with a particle size of 15–45 μm were sieved and divided for the SLM process. Specimens with dimensions of 10 mm × 10 mm × 3 mm were produced using SLM in an argon environment with an AM system (LUMEX Avance-25, Higashimorida, Fukui, Japan). Several parameters, including the laser power and the scan speed, were employed with a layer thickness of 50 μm. A scan strategy with a bidirectional scanning vector and 90° rotation between consecutive layers was applied. The effect of the SLM process on the microstructure of the Ti-based bulk metallic glass was investigated using XRD and TEM.

3. Results and Discussion

3.1. High Glass-Forming Ability for Ti-Based Metallic Glass

Several empirical and theoretical criteria for an easy MG formation were indicated by the findings. These criteria deal with electronic, topological, compositional, kinetic, and thermodynamic conditions that facilitate the formation of a short-range-order structure. They include Turnbull's deep eutectic rule and Egami's atomic size rule [45,46]. Based on the deep eutectic rule, the alloys with lower T_l would inherently have a higher GFA because the nucleation and growth of the crystalline phase is directly related to the cooling temperature and time. Alloys with lower T_l temperatures are in a liquid state at lower temperatures, making the rapidly cooled melt's transformation into a crystalline phase more difficult. Therefore, an alloy composition at or near the deep eutectic point becomes easier to transform into the glassy phase before forming the crystalline seed [47]. Using the physical concept of strong binary eutectic clusters as a basis, Lu et al. [48,49] proposed the following equation to identify the deep eutectic composition:

$$C_{am} = \alpha\,(Eu_{A\text{-}B1}) + \beta\,(Eu_{A\text{-}B2}) \tag{1}$$

$$\alpha\Delta H_{A\text{-}B1} = \beta\Delta H_{A\text{-}B2}, \tag{2}$$

where C_{am} indicates a composition range bounded by the two deep binary eutectic compositions, $Eu_{A\text{-}B}$ is the eutectic point for the binary cluster A-B, $\Delta H_{A\text{-}B}$ is the mixing heat for the binary cluster A-B, α and β are constants, and α + β = 1. Ti, Zr, Co, and Si can form the binary deep eutectics $Ti_{77}Co_{23}$, $Ti_{86}Si_{14}$, $Zr_{91.2}Si_{8.8}$, and $Zr_{78.5}Co_{21.5}$ [50]. The mixing heats for the atom pairs of Ti–Co, Ti–Si, Zr–Si, and Zr–Co are −28, −66, −84, and −41 kJ/mole, respectively [51]. Following Equations (1) and (2), the possible eutectic compositions (C_{am}) in the $Ti_{42}Ta_3(Zr\text{–}Si\text{–}Co)$ system can be calculated, and they yield a composition of $Ti_{42}Zr_{37.8}Si_{3.2}Co_{14}Ta_3$. Figure 1 presents the GFA factors of the melt-spun

$Ti_{42}Ta_3$(Zr–Si–Co) ribbons, which included the liquidus temperature (T_l) (Figure 1a), supercooled liquid region ($\Delta T_x = T_x - T_g$) (Figure 1b), GFA index [$\gamma_m = (2T_x - T_g)/T_l$)] (Figure 1c), and GFA index [$\gamma = T_x/(T_g + T_l)$] (Figure 1d). Figure 2 presents the XRD pattern of the melt-spun $Ti_{42}Ta_3$(Zr–Si–Co) ribbons with various compositions. As evidenced in Figures 1 and 2, the XRD pattern of the predicted composition exhibited a broad diffuse peak with a nanocrystalline peak, implying that some physical properties were neglected. We attempted to measure various parameters of the predicted alloy near the eutectic compositions. The true eutectic point clearly shifted into a lower Zr and Co but higher Si content (i.e., $Ti_{42}Zr_{32.5}Si_{12.5}Co_{10}Ta_3$). The glassy alloys had better ΔT_x, γ_m, and γ values between the true and predicted composition, suggesting that a lower Si content is a necessity. Because the gas atomization process requires a metallic liquid with good fluidity that can be impinged on by high-pressure inert gas jets into fine metal droplets, the optimal composition is $Ti_{42}Zr_{35}Si_5Co_{15}Ta_3$.
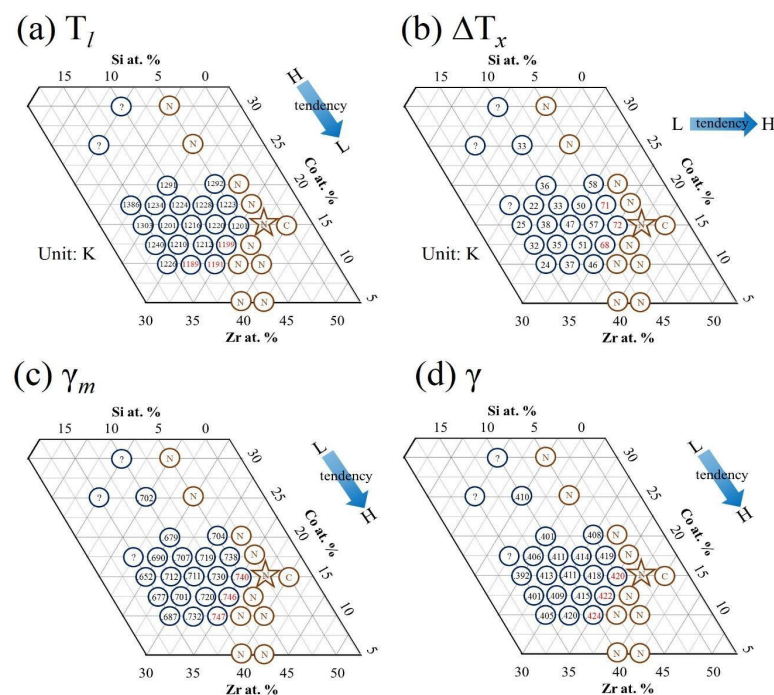

Figure 1. Composition diagram for $Ti_{42}Ta_3$-Zr-Co-Si alloy ribbon. A star symbol indicates predicted composition using the calculation of binary eutectic clusters. An *N* indicates that the XRD pattern of ribbon exhibited a broad diffuse peak with a nanocrystalline peak. A *C* indicates a very sharp crystalline peak. The other compositions are of the MG structure. (**a**) Liquidus temperature, T_l, (**b**) supercooled liquid region, ΔT_x, (**c**) GFA index, γ_m, and (**d**) GFA index, γ.

The alloy composition was further fine-tuned through the substitution of Co with Sn in $Ti_{42}Zr_{35}Si_5Co_{15-x}Sn_xTa_3$. Using Egami's atomic size rule, we selected Sn as the alloying element for the following reasons. (1) The difference in atomic size between Sn and the constituent elements is large; the atomic radius of Sn is larger than the radii of Ti, Zr, Si, and Co by 1.2–30%. (2) Sn and Si belong to the same family in the periodic table, and the number of valence electrons of Sn is the same as that of Si. (3) Sn is a biofriendly element. Figure 3 illustrates the DSC curve of the $Ti_{42}Zr_{35}Si_5Co_{15-x}Sn_xTa_3$ melt-spun alloy ribbons. The thermal parameters of T_g, T_x, ΔT_x, T_l, γ, and γ_m are summarized in Table 1. According to the results of DSC analysis, the highest ΔT_x value (81 K) and a relatively high γ (0.427) and γ_m (0.763) occurred in the $Ti_{42}Zr_{35}Si_5Co_{12.5}Sn_{2.5}Ta_3$, which would allow the alloy to retain a high GFA.
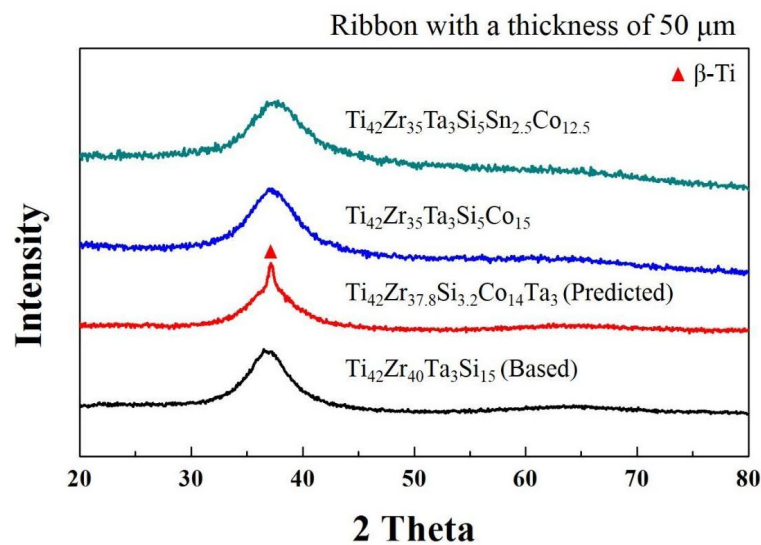
Ribbon with a thickness of 50 μm

Figure 2. XRD patterns of Ti–Zr–Ta–Si–Sn–Co melt-spun ribbons.

Ribbon with a thickness of 50 μm
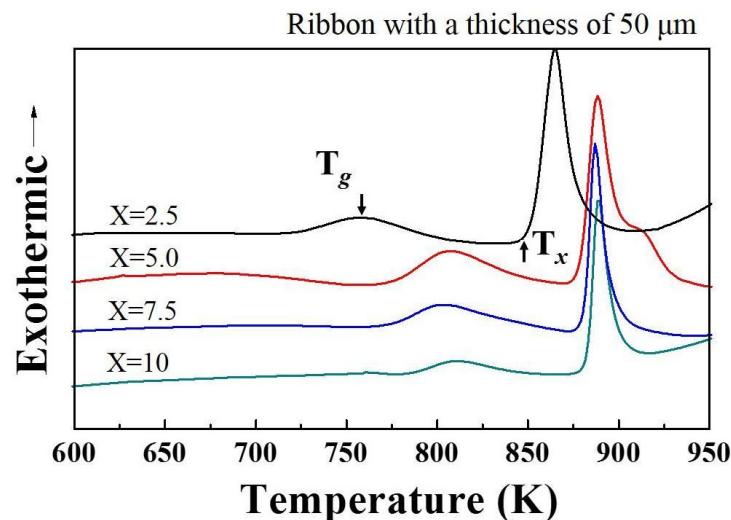
Figure 3. DSC curves for $Ti_{42}Zr_{35}Si_5Co_{15-x}Sn_xTa_3$ (x = 2.5–10 in at %) glassy alloy ribbons, respectively.

Table 1. Thermal properties of as-quenched base $Ti_{42}Zr_{40}Ta_3Si_{15}$ and other newly designed alloys with various combinations of Sn and Co additions.

Alloys	T_g(K)	T_x(K)	ΔT_x(K)	T_l(K)	γ	γ_m
Base $Ti_{42}Zr_{40}Si_{15}Ta_3$	799	898	99	1728	0.355	0.577
$Ti_{42}Zr_{35}Si_5Co_{15}Ta_3$	745	817	72	1201	0.420	0.740
$Ti_{42}Zr_{35}Si_5Co_{12.5}Sn_{2.5}Ta_3$	761	842	81	1210	0.427	0.763
$Ti_{42}Zr_{35}Si_5Co_{10}Sn_5Ta_3$	809	873	64	1212	0.432	0.773
$Ti_{42}Zr_{35}Si_5Co_{7.5}Sn_{7.5}Ta_3$	803	874	71	1198	0.437	0.789
$Ti_{42}Zr_{35}Si_5Co_{2.5}Sn_{12.5}Ta_3$	815	874	59	1200	0.434	0.778

3.2. Gas Atomization Process

A master ingot with a nominal composition of $Ti_{42}Zr_{35}Si_5Co_{12.5}Sn_{2.5}Ta_3$ (in at. %) was melted in an induction vacuum furnace. High-pressure inert gas jets were impinged into fine metal droplets. The droplets settled by gravity or cyclonic separation at the bottom of the chamber to form the powder. The morphology of atomized powders, displayed in Figure 4, presents a typical spherical shape and smooth surface for the majority of powders. Only a few powders had satellite particles or an elongated shape. A cross-sectional

metallography of the atomized powders clearly showed the homogenous and feature-less microstructure of the solid particles. The particle size distribution of the powders is displayed in Figure 5. In addition, the yield rate for the resulting powders with a size of 15–45 μm was more than 50%. It represented the gas atomization production conditions as being finally mature and showed the fact that they would soon enter the stage of mass production. Based on systematic XRD characterization, as presented in Figure 6, $Ti_{42}Zr_{35}Si_5Co_{12.5}Sn_{2.5}Ta_3$ exhibited a dominant amorphous phase with a nanocrystalline peak, especially in powders smaller than 25 μm. The DSC analyses were conducted on gas-atomized $Ti_{42}Zr_{35}Si_5Sn_{2.5}Co_{12.5}Ta_3$ powders of different powder size ranges (<25, 25–37, 37–44, and 44–53 μm) compared with the fully amorphous ribbons prepared by melt spinning, as indicated in Figure 7. All specimens revealed characteristics of fully or partially amorphous alloys, with T_g and T_x and an exothermal hump over the supercooled viscous regime. We could estimate the fraction of amorphous phase from the crystallization's exothermic peak of energy by comparing the fully amorphous state (100%) of the melt-spun ribbons. The volume fractions of the amorphous phase in the atomized $Ti_{42}Zr_{35}Si_5Sn_{2.5}Co_{12.5}Ta_3$ powders were 73% (<25 μm), 61% (25–37 μm), 50% (37–44 μm), and 31% (44–53 μm), respectively. The cooling rate of the gas atomization process was estimated to be approximately 10^2 K/s, and the cooling rate of a typical SLM process was estimated to be greater than 10^3 K/s [5]. Therefore, the current atomized powders can be expected to contain a higher degree of amorphous-phase volume fraction after laser remelting.
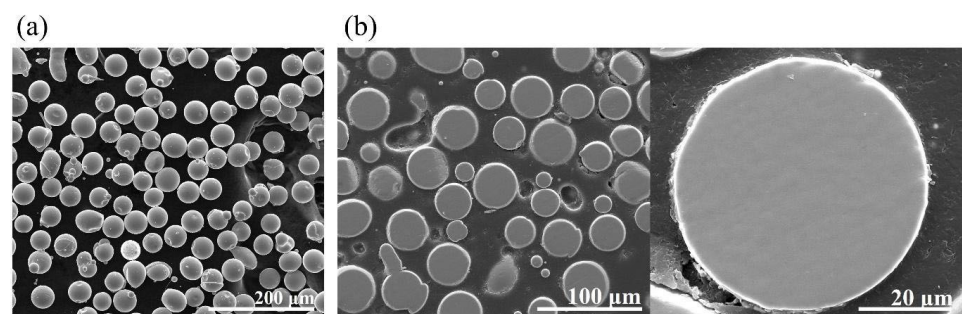
(a)   (b)

Figure 4. (**a**) Morphology of atomized alloy powders observed using SEM. (**b**) Cross-sectional metallography of the atomized $Ti_{42}Zr_{35}Si_5Co_{12.5}Sn_{2.5}Ta_3$ alloy powder.
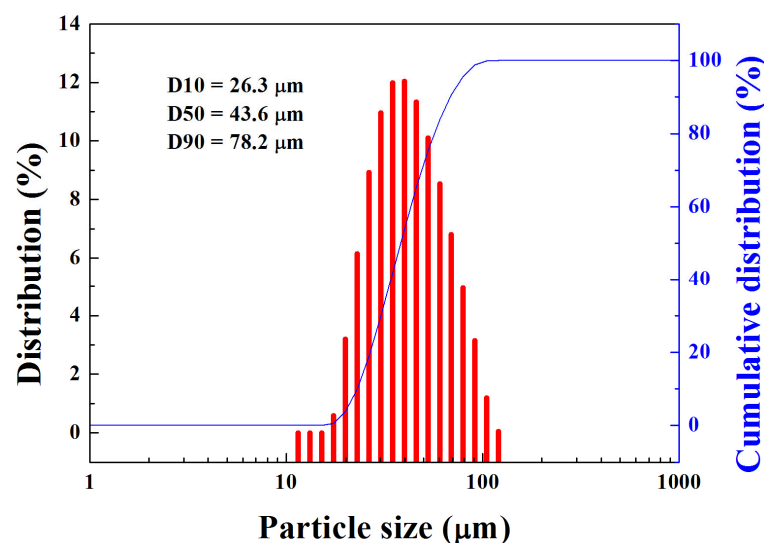
Figure 5. Plots of particle size distribution for as-atomized $Ti_{42}Zr_{35}Si_5Co_{12.5}Sn_{2.5}Ta_3$ powders.
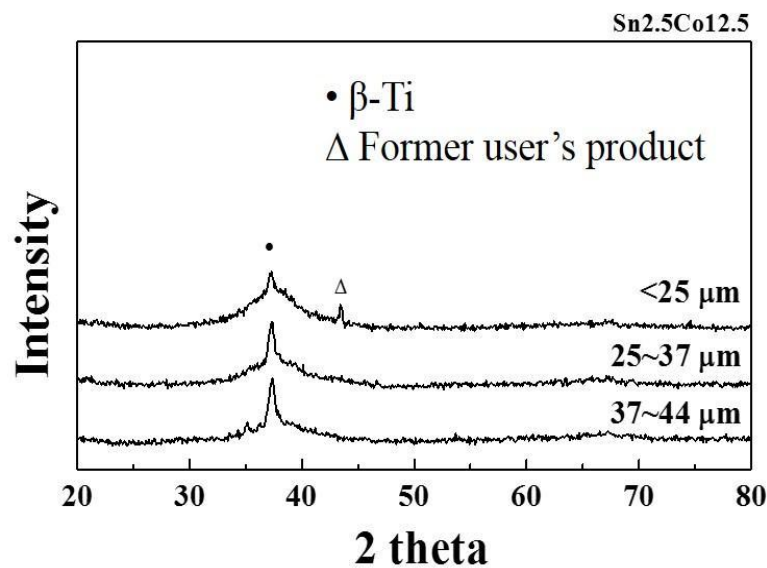
Figure 6. XRD patterns of atomized alloy powders for different particle size ranges.
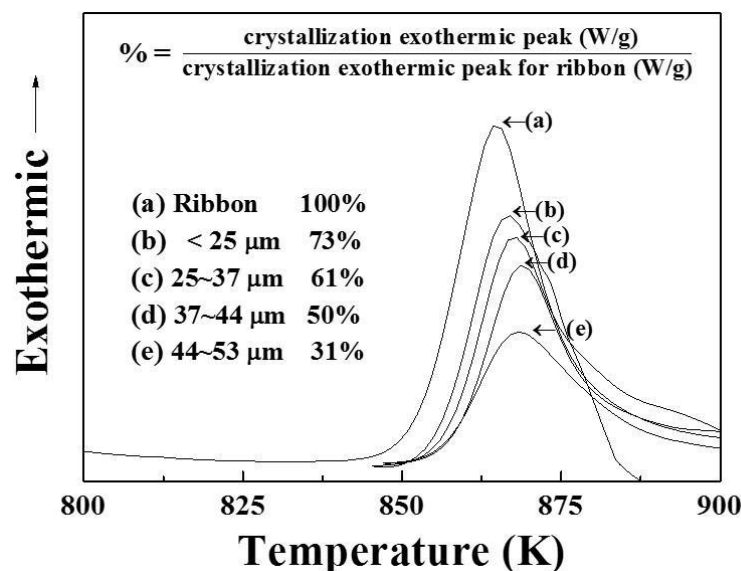

Figure 7. DSC curves of gas-atomized powders with different sizes and ribbons.

3.3. Selective Laser Melting

For the analysis, the formation and microstructure were made with different laser energy densities (in J/mm^2) $E\rho = P/VD$, where P is the laser power (in W), V is the scan rate (in mm/s), and D is the beam size (in μm). The gas-atomized powders with a particle size between 15 and 45 μm were examined using laser remelting for the line, plan, and volume. Figure 8 illustrates the appearance of a line formation with different laser parameters. Alloy powder easily formed an integral and continuous alloy line at the scan rate of <800 mm/s. At such a high scan speed, the powder was unable to receive sufficient energy during SLM processing, leading to incomplete melting and poor interparticle bonding. The XRD patterns for "plane" samples fabricated using different laser energy densities with a 10–40% overlap are displayed in Figure 9, with overlap occurring where an XRD pattern covered another by the crossing of its line-width edge. The crystallization rate was noticeably proportional to the overlap (Figure 9a,b) and laser energy density (Figure 9c,d), suggesting that a lower laser energy density is necessary. The energy in the laser beam heat-affected zone (HAZ) ought to be lower than that within and between the layers of the crystallization barrier for MG but must still have suitable energy levels to connect

neighboring powders in order to form continuous products, as illustrated in Figure 10. This suggests that the optimal laser parameters are a scan rate of 600 mm/s, a power of 120 W, and an overlap of 10%. Figure 11 displays the bright- and dark-field TEM image of the as-built $Ti_{42}Zr_{35}Si_5Co_{12.5}Sn_{2.5}Ta_3$ bulk metallic glass. The selected area's diffraction patterns corresponding to the zone axis $(01\bar{1}0)$ of the hcp-α-Ti-type and amorphous structure are displayed in Figure 11b,c, respectively. This pattern indicates that the as-built sample by SLM is in a composite state. When comparing the cooling rate of the gas atomization process (10^2 K/s) with the cooling rate of the SLM process ($>10^3$ K/s) [5], we expected to observe a higher amorphous-phase volume fraction in the SLM block than in the atomized powder (the volume fraction of the atomized powders was 50–73%). However, the volume fraction of the amorphous phase in the SLM block was only 40–50%, according to the TEM image analysis (Figure 11a). This suggests that the partial crystallization of the SLM block was induced by the HAZ or the repeated thermal cycle during the laser remelting of each new layer.
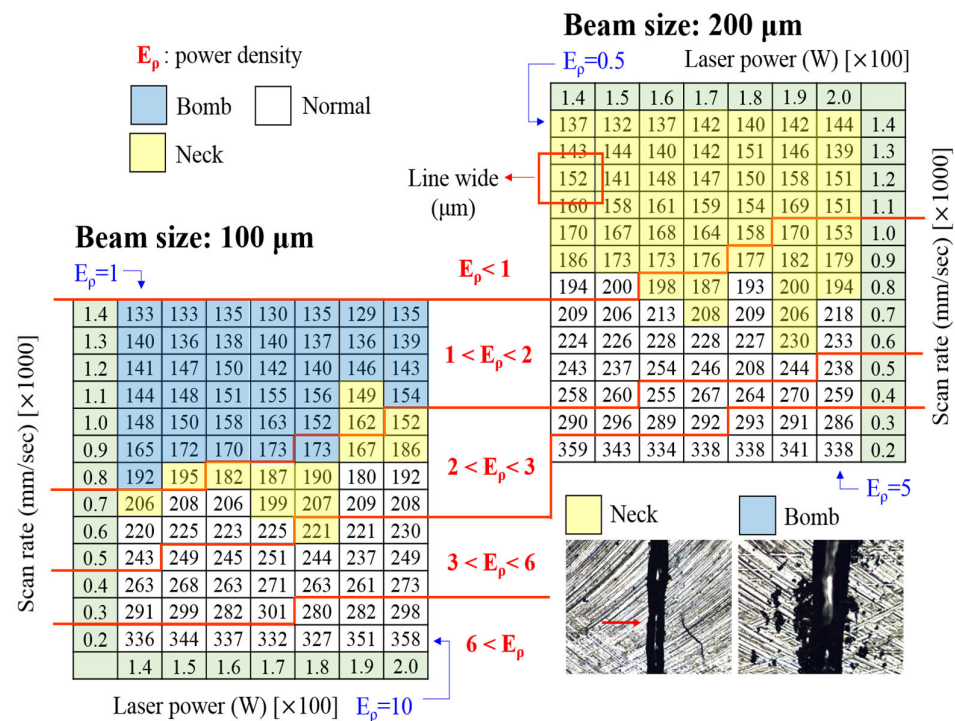
Beam size: 200 μm — Laser power (W) [×100], Scan rate (mm/sec) [×1000]

1.4	1.5	1.6	1.7	1.8	1.9	2.0	
137	132	137	142	140	142	144	1.4
143	144	140	142	151	146	139	1.3
152	141	148	147	150	158	151	1.2
160	158	161	159	154	169	151	1.1
170	167	168	164	158	170	153	1.0
186	173	173	176	177	182	179	0.9
194	200	198	187	193	200	194	0.8
209	206	213	208	209	206	218	0.7
224	226	228	228	227	230	233	0.6
243	237	254	246	208	244	238	0.5
258	260	255	267	264	270	259	0.4
290	296	289	292	293	291	286	0.3
359	343	334	338	338	341	338	0.2

E_ρ: power density. Bomb / Normal / Neck. $E_\rho=0.5$. Line wide (μm). $E_\rho=5$.

Beam size: 100 μm — Scan rate (mm/sec) [×1000]

$E_\rho=1$

1.4	133	133	135	130	135	129	135
1.3	140	136	138	140	137	136	139
1.2	141	147	150	142	140	146	143
1.1	144	148	151	155	156	149	154
1.0	148	150	158	163	152	162	152
0.9	165	172	170	173	173	167	186
0.8	192	195	182	187	190	180	192
0.7	206	208	206	199	207	209	208
0.6	220	225	223	225	221	221	230
0.5	243	249	245	251	244	237	249
0.4	263	268	263	271	263	261	273
0.3	291	299	282	301	280	282	298
0.2	336	344	337	332	327	351	358
	1.4	1.5	1.6	1.7	1.8	1.9	2.0

Laser power (W) [×100] $E_\rho=10$

$E_\rho<1$; $1<E_\rho<2$; $2<E_\rho<3$; $3<E_\rho<6$; $6<E_\rho$

Neck   Bomb

Figure 8. OM images of alloy lines formed after laser remelting at different energy densities for $Ti_{42}Zr_{35}Si_5Sn_{2.5}Co_{12.5}Ta_3$ (color online).

The SLM process includes the remelting and solidification of the metallic powders. When the cooling rate is fast enough to suppress crystallization behavior, an MG can be formed. The high GFA of the alloy composition contributes greatly to this. Additionally, inattention to the HAZ may result in crystallization because of the limited thermal stability of the amorphous alloy's crystallization temperature. This problem may be overcome by decreasing the substrate temperature and reducing the HAZ's adverse effects or by changing the laser scan strategy to avoid heat clustering as much as possible.
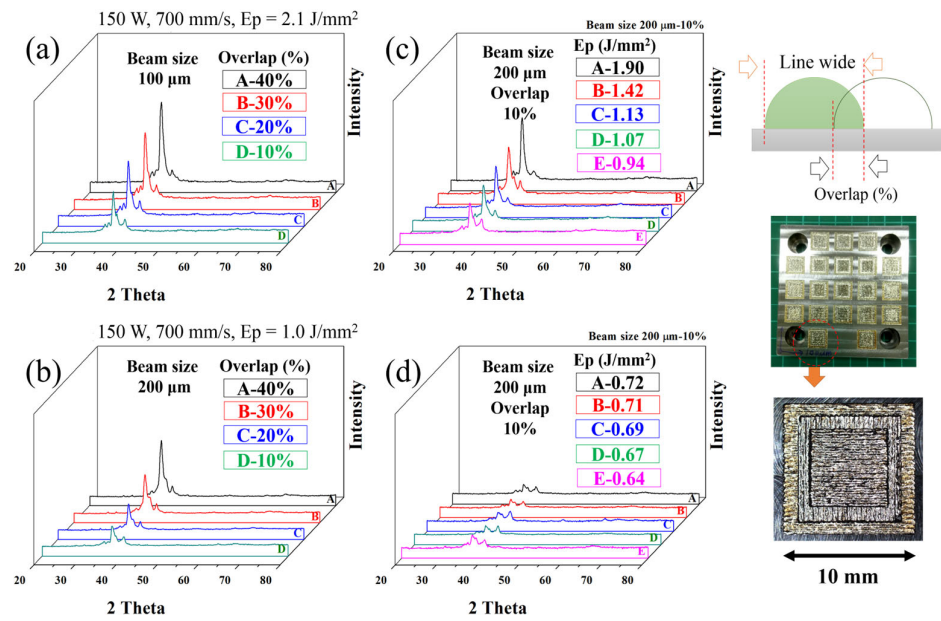
Figure 9. XRD pattern of SLM-plane-type samples at (**a**) beam size 100 μm, 150 W, 700 mm/s (Eρ = 2.1 J/mm^2) with 10–40% overlaps, (**b**) beam size 200 μm, 150 W, 700 mm/s with 10–40% overlaps, (**c**) Eρ = 0.94–1.90 J/mm^2 with 10% overlap, and (**d**) Eρ = 0.64–0.72 J/mm^2 with 10% overlap.
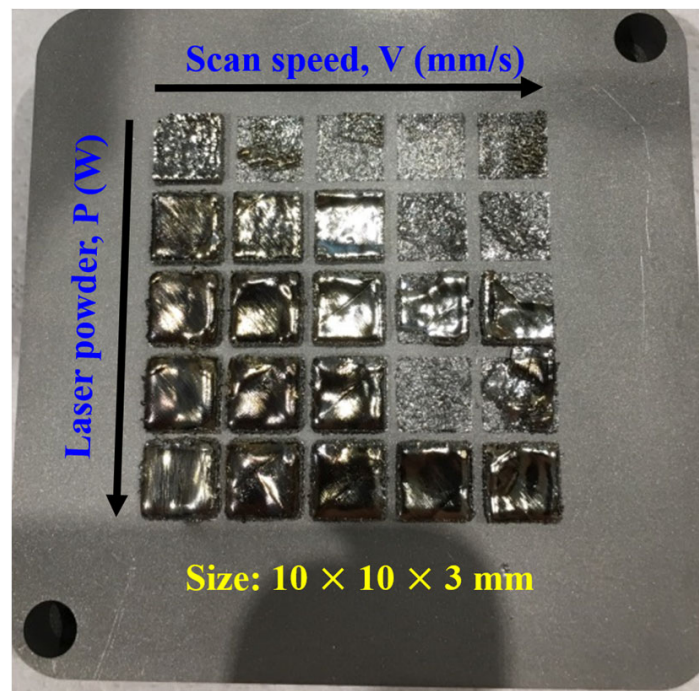
Figure 10. Top-view photographs of SLM volume samples.

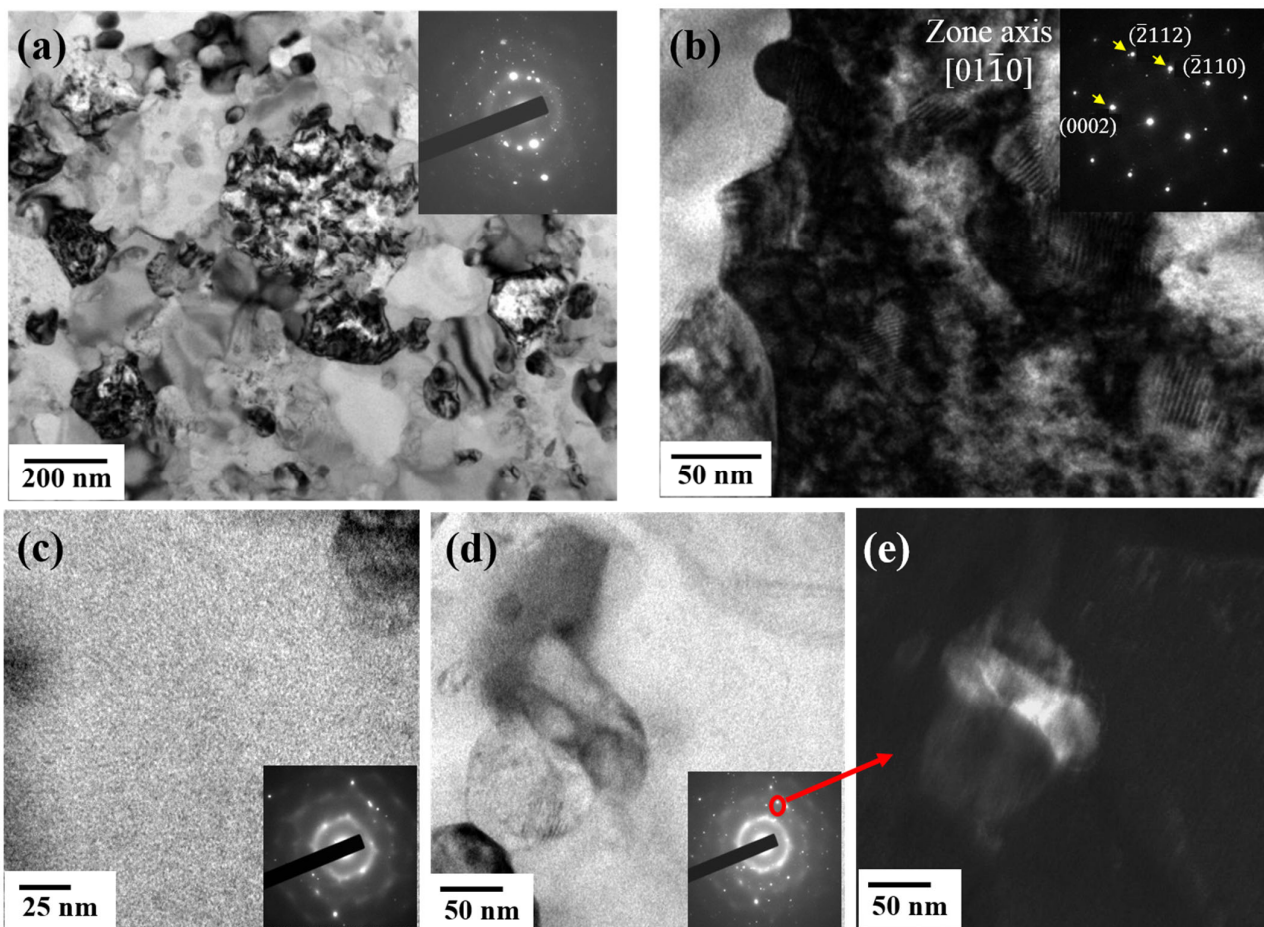**Figure 11.** TEM image of $Ti_{42}Zr_{35}Si_5Co_{12.5}Sn_{2.5}Ta_3$ bulk metallic glass composite at scan rate of 600 mm/s, power of 120 W and overlap of 10%: (**a**) bright-field TEM image with inserted selected area diffraction (SAD) pattern for hybrid of crystalline and amorphous phase. (**b**) High-resolution image magnified from (**a**); the image illustrates that the crystalline phase has an hcp-α-Ti-type structure. (**c**) Bright-field image and SAD of amorphous phase. (**d,e**) Bright- and dark-field image of crystalline particle embedded in amorphous matrix.

4. Conclusions

The $Ti_{42}Zr_{35}Si_5Co_{12.5}Sn_{2.5}Ta_3$ BMGC has been successfully fabricated by SLM. The influence of the processing parameters on the microstructure of the fabricated ribbon, powder, and BMGCs was systematically investigated. This study makes the following contributions.

1. A new biocompatible Ti-based MG, $Ti_{42}Zr_{35}Si_5Co_{12.5}Sn_{2.5}Ta_3$, with high GFA was synthesized. The glassy alloy exhibited a relatively high thermal stability with a supercooled liquid region (ΔT_x) above 81 K. The T_g, T_x, T_l, γ, and γ_m were 761 K, 842 K, 1210 K, 0.427, and 0.763, respectively.
2. The morphology of the atomized powders presented a typical spherical shape and smooth surface for the majority of the powder. When subject to systematic XRD characterization, the powder exhibited a dominant amorphous phase with some nanocrystalline peaks. The volume fractions of the amorphous phase in the atomized $Ti_{42}Zr_{35}Si_5Sn_{2.5}Co_{12.5}Ta_3$ powders characterized by DSC were 73% (<25 μm), 61% (25–37 μm), 50% (37–44 μm), and 31% (44–53 μm), respectively.
3. The gas-atomized powders with a particle size between 15 and 45 μm were examined by laser remelting for the line, plan, and volume. Achieving a lower laser energy density was a top priority because the energy in the laser beam HAZ ought to be lower than the crystallization barrier for MG within and between layers but must

still have a suitable energy level to connect neighboring powders in order to form continuous products. The optimal laser parameters are a scan rate of 600 mm/s, a power of 120 W, and an overlap of 10%.

4. The microstructure of biocompatible Ti-based bulk metallic glass composites for additive manufacturing consists of an hcp-α-Ti-type and amorphous structure.

SLM technology offers an opportunity to manufacture a range of new products. Because Ti-based MG exhibits good biocompatible properties, the complex, customizable, and fast-yield products of Ti-based BMGC by SLM are promising candidates for biomedical implants.

References

1. Gibson, I.; Rosen, D.; Stucker, B.; Khorasani, M. *Additive Manufacturing Technologies*; Springer: Berlin/Heidelberg, Germany, 2021. [CrossRef]
2. Kirihara, S.; Nakata, K. *Multi-Dimensional Additive Manufacturing*; Springer: Berlin/Heidelberg, Germany, 2021. [CrossRef]
3. Zhu, J.; Zhou, H.; Wang, C.; Zhou, L.; Yuan, S.; Zhang, W. A review of topology optimization for additive manufacturing: Status and challenges. *Chin. J. Aeronaut.* **2021**, *34*, 91. [CrossRef]
4. Gu, D.D.; Meiners, W.; Wissenbach, K.; Poprawe, R. Laser additive manufacturing of metallic components: Materials, processes and mechanisms. *Int. Mater. Rev.* **2012**, *57*, 133. [CrossRef]
5. Pauly, S.; Wang, P.; Kuhn, U.; Kosiba, K. Experimental determination of cooling rates in selectively laser-melted eutectic Al-33Cu. *Addit. Manuf.* **2018**, *22*, 753. [CrossRef]
6. Bahl, S.; Mishra, S.; Yazar, K.U.; Kola, I.R.; Chatterjee, K.; Suwas, S. Non-equilibrium microstructure, crystallographic texture and morphological texture synergistically result in unusual mechanical properties of 3D printed 316L stainless steel. *Addit. Manuf.* **2019**, *28*, 65. [CrossRef]
7. Fereiduni, E.; Ghasei, A.; Eibestawi, M. Selective laser melting of hybrid ex-situ/in-situ reinforced titanium matrix composites: Laser/powder interaction, reinforcement formation mechanism, and non-equilibrium microstructural evolutions. *Mater. Des.* **2019**, *184*, 108185. [CrossRef]
8. Mohammed, M.T. Mechanical Properties of SLM-Titanium Materials for Biomedical Applications: A Review. *Mater. Today Proc.* **2018**, *5*, 17906. [CrossRef]
9. Culmone, C.; Smit, G.; Breedveld, P. Additive manufacturing of medical instruments: A state-of-the-art review. *Addit. Manuf.* **2019**, *27*, 461. [CrossRef]
10. Tilton, M.; Lewis, G.S.; Manogharan, G.P. *Additive Manufacturing of Orthopedic Implants*; Springer: Berlin/Heidelberg, Germany, 2018. [CrossRef]
11. Wu, T.; Yu, S.; Chen, D.; Wang, Y. Bionic design, materials and performance of bone tissue scaffolds. *Materials* **2017**, *10*, 1187. [CrossRef]
12. Burnard, J.L.; Parr, W.C.H.; Choy, W.J.; Walsh, W.R.; Mobbs, R.J. 3D-printed spine surgery implants: A systematic review of the efficacy and clinical safety profile of patient-specific and off-the-shelf devices. *Eur. Spine J.* **2020**, *29*, 1248. [CrossRef] [PubMed]
13. Javaid, M.; Haleem, A. Current status and applications of additive manufacturing in dentistry: A literature-based review. *J. Oral Biol. Craniofacial Res.* **2019**, *9*, 179. [CrossRef]
14. Qu, H. Additive manufacturing for bone tissue engineering scaffolds. *Mater. Today Commun.* **2020**, *24*, 101024. [CrossRef]

15. Ivanova, E.P.; Bazaka, K.; Crawford, R.J. Cytotoxicity and biocompatibility of metallic biomaterials. *New Funct. Biomater. Med. Healthc.* **2014**, *6*, 148.

16. Prasad, K.; Bazaka, O.; Chua, M.; Rochford, M.; Fedrick, L.; Spoor, J.; Symes, R.; Tieppo, M.; Collins, C.; Cao, A.; et al. Metallic biomaterials: Current challenges and opportunities. *Materials* **2017**, *10*, 884. [CrossRef]

17. Gobbi, S.J.; Gobbi, V.J.; Rocha, Y. Requirements for selection / development of a biomaterial. *J. Sci. Tech. Res.* **2019**, *14*, 10647. [CrossRef]

18. Balakrishnan, P.; Thomas, S.; Sadasivan, S.M. *Fundamental Biomaterials: Metals*; Woodhead: Sawston, UK, 2018. [CrossRef]

19. Basu, B.; Katti, D.S.; Kumar, A. *Advanced Biomaterials: Fundamentals, Processing, and Applications*; Wiley: Hoboken, NJ, USA, 2009; ISBN 978-0-470-19340-2.

20. Niinomi, M. *Metals for Biomedical Devices*; Woodhead: Sawston, UK, 2010; ISBN 9780081026663.

21. Geetha, M.; Singh, A.K.; Asokamani, R.; Gogia, A.K. Ti based biomaterials, the ultimate choice for orthopedic implants—A review. *Prog. Mater. Sci.* **2009**, *54*, 397. [CrossRef]

22. Kaur, M.; Singh, K. Review on titanium and titanium-based alloys as biomaterials for orthopedic applications. *Mater. Sci. Eng. C* **2019**, *102*, 844. [CrossRef] [PubMed]

23. Dearnley, P.A.; Dahm, K.L.; Çimeno, H. The corrosion–wear behaviour of thermally oxidised CP-Ti and Ti–6Al–4V. *Wear* **2004**, *256*, 469. [CrossRef]

24. Khan, M.A.; Williams, R.L.; Williams, D.F. Conjoint corrosion and wear in titanium alloys. *Biomaterials* **1999**, *20*, 765. [CrossRef]

25. Jacobs, J.J.; Gilbert, J.L.; Urban, R.M. Current Concepts Review-Corrosion of Metal Orthopedic Implants. *J. Bone Jt. Surg. Am.* **1998**, *80*, 268. [CrossRef] [PubMed]

26. Khan, M.A.; Williams, R.L.; Williams, D.F. In-vitro corrosion and wear of titanium alloys in the biological environment. *Biomaterials* **1996**, *17*, 2117. [CrossRef]

27. Okazakia, Y.; Gotohb, E. Comparison of metal release from various metallic biomaterials in vitro. *Biomaterials* **2005**, *26*, 11. [CrossRef] [PubMed]

28. Festas, A.; Ramos, A.; Davim, J.P. Machining of titanium alloys for medical application—A review. *Proc. Inst. Mech. Eng. Part B J. Eng. Manuf.* **2022**, *236*, 309–318. [CrossRef]

29. Hu, M.; Wang, L.; Li, G.; Huang, Q.; Liu, Y.; He, J.; Wu, H.; Song, M. Investigations on microstructure and properties of Ti-Nb-Zr medium-entropy alloys for metallic biomaterials. *Intermetallics* **2022**, *145*, 107568. [CrossRef]

30. Hori, T.; Nagase, T.; Todai, M.; Matsugaki, A.; Nakano, T. Development of non-equiatomic Ti-Nb-Ta-Zr-Mo high-entropy alloys for metallic biomaterials. *Scr. Mater.* **2019**, *172*, 83–87. [CrossRef]

31. Jiménez-Marcos, C.; Baltatu, M.S.; Florido-Suárez, N.R.; Socorro-Perdomo, P.P.; Vizureanu, P.; Mirza-Rosca, J.C. Mechanical properties and corrosion resistance of two new titanium alloys for orthopaedics applications. *Mater. Today Proc.* **2023**, *72*, 544–549. [CrossRef]

32. Pradeep, N.B.; Hegde, M.R.; Patel, G.M.; Giasin, K.; Pimenov, D.Y.; Wojciechowski, S. Synthesis and characterization of mechanically alloyed nanostructured ternary titanium based alloy for bio-medical applications. *J. Mater. Res. Technol.* **2022**, *16*, 88–101. [CrossRef]

33. Tshephe, T.S.; Akinwamide, S.O.; Olevsky, E.; Olubambi, P.A. Additive manufacturing of titanium-based alloys—A review of methods, properties, challenges, and prospects. *Heliyon* **2022**, *8*, e09041. [CrossRef]

34. Zhu, S.L.; Wang, X.M.; Qin, F.X.; Inoue, A. A new Ti-based bulk glassy alloy with potential for biomedical application. *Mater. Sci. Eng. A* **2007**, *459*, 233. [CrossRef]

35. Tsai, P.H.; Lin, Y.Z.; Li, J.B.; Jian, S.R.; Jang, J.S.C.; Li, C.; Chu, J.P.; Huang, J.C. Sharpness improvement of surgical blade by means of ZrCuAlAgSi metallic glass and metallic glass thin film coating. *Intermetallics* **2012**, *31*, 127. [CrossRef]

36. Lin, C.H.; Huang, C.H.; Chuang, J.F.; Lee, H.C.; Liu, M.C.; Du, X.H.; Huang, J.C.; Jang, J.S.C.; Chen, C.H. Simulated body-fluid tests and electrochemical investigations on biocompatibility of metallic glasses. *Mater. Sci. Eng. C* **2012**, *32*, 2578. [CrossRef]

37. Li, J.B.; Lin, H.C.; Jang, J.S.C.; Kuo, C.N.; Huang, J.C. Novel open-cell bulk metallic glass foams with promising characteristics. *Mater. Lett.* **2013**, *105*, 140. [CrossRef]

38. Lin, C.H.; Huang, C.H.; Chuang, J.F.; Huang, J.C.; Jang, J.S.C.; Chen, C.H. Rapid screening of potential metallic glasses for biomedical applications. *Mater. Sci. Eng. C* **2013**, *33*, 4520. [CrossRef]

39. Oak, J.J.; Inoue, A. Attempt to develop Ti-based amorphous alloys for biomaterials. *Mater. Sci. Eng. A* **2007**, *220*, 449–451. [CrossRef]

40. Brothers, A.H.; Dunand, D.C. Amorphous metal foams. *Scr. Mater.* **2006**, *54*, 513. [CrossRef]

41. Lin, H.C.; Tsai, P.H.; Ke, J.H.; Li, J.B.; Jang, J.S.C.; Huang, C.H.; Huang, J.C. Designing a toxic-element-free Ti-based amorphous alloy with remarkable supercooled liquid region for biomedical application. *Intermetallics* **2014**, *55*, 22. [CrossRef]

42. Huang, L.; Qiao, D.; Green, B.A.; Liaw, P.K.; Wang, J.; Pang, S.; Zhang, T. Bio-corrosion study on zirconium-based bulk-metallic glasses. *Intermetallics* **2009**, *17*, 195. [CrossRef]

43. Tsai, P.H.; Xiao, A.C.; Li, J.B.; Jang, J.S.C.; Chu, J.P.; Huang, J.C. Prominent Fe-based bulk amorphous steel alloy with large supercooled liquid region and superior corrosion resistance. *J. Alloys Compd.* **2014**, *586*, 94. [CrossRef]

44. Ma, C.; Du, T.; Niu, X.; Fan, Y. Biomechanics and mechanobiology of the bone matrix. *Bone Res.* **2022**, *10*, 59. [CrossRef]

45. Cohen, M.H.; Turnbull, D. Composition Requirements for Glass Formation in Metallic and Ionic Systems. *Nature* **1961**, *189*, 131. [CrossRef]

46. Egami, T.; Waseda, Y. Atomic size effect on the formability of metallic glasses. *J. Non-Cryst. Solids* **1984**, *64*, 113. [CrossRef]

47. Wang, D.; Li, Y.; Sun, B.B.; Sui, M.L.; Lu, K.; Ma, E. Bulk metallic glass formation in the binary Cu-Zr system. *Appl. Phys. Lett.* **2004**, *84*, 4029. [CrossRef]

48. Lu, Z.P.; Shen, J.; Xing, D.W.; Sun, J.F.; Liu, C.T. Binary eutectic clusters and glass formation in ideal glass forming liquids. *Appl. Phys. Lett.* **2006**, *89*, 071910. [CrossRef]

49. Lu, Z.P.; Shen, J.; Xing, D.W.; Sun, J.F.; Liu, C.T. Ti–Zr–Be ternary bulk metallic glasses correlated with binary eutectic clusters. *Mater. Sci. Eng. A* **2010**, *527*, 6248.

50. Massalski, T.B.; Okamoto, H.; Subramanian, P.R.; Kacprzak, L. *Binary Phase Diagram*, 2nd ed.; ASM International: Novelty, OH, USA, 1996.

51. Takeuchi, A.; Inoue, A. Classification of bulk metallic glasses by atomic size difference, heat of mixing and period of constituent elements and its application to characterization of the main alloying element. *Mater. Trans.* **2005**, *46*, 2817. [CrossRef]